Chemical Science

ROYAL SOCIETY OF CHEMISTRY

EDGE ARTICLE

View Article Online
View Journal | View Issue

Cite this: *Chem. Sci.*, 2025, **16**, 753

All publication charges for this article have been paid for by the Royal Society of Chemistry

Reconstructing the phase of vanadium oxides enables redox-catalysis manipulated reversible sulfur conversion for stable Zn–S batteries†

Hao Luo, ‡*[ae] Fan Li,‡[ab] Mingli Wang,*[d] Shang Sun,[b] Min Zhou,[b] Wenjing Zhang,[b] Hengrui Guo,[ae] Xueyin Su,[ae] Xiaolong Li*[c] and Lina Ma *[b]

The naturally sluggish redox kinetics and limited utilization associated with the sulfur conversion in Zn/S electrochemistry hinder its real application. Herein, we report an *in situ* phase reconstruction strategy that activates the catalytic activity of vanadium oxides for invoking redox-catalysis to manipulate reversible sulfur conversion. It was identified that the V_2O_3@C/S precursor derived from metal organic frameworks could be transformed into $V_2O_{5-m}{\cdot}nH_2O$@C/S by a facile electrochemical induction process. Vanadium oxides can realize a faster zinc ion storage process than sulfur components during the discharging process, thereby the pre-zincified $Zn_xV_2O_5{\cdot}nH_2O$ behaves as a redox medium to catalyze the sulfur reduction *via* a spontaneous reaction ($Zn_{x+1}V_2O_5 + S = Zn_xV_2O_5 + ZnS$, $\Delta G = -6.4$ kJ mol^{-1}). For the reverse battery recharging, the electrodeposited ZnS around the active sites can be easily activated and the facile Zn^{2+} transport between $Zn_xV_2O_5{\cdot}nH_2O$ and ZnS enables the reversible conversion of ZnS back to S ($Zn_xV_2O_5 + ZnS = Zn_{x+1}V_2O_5 + S$, $\Delta G = -7.02$ kJ mol^{-1}). Accordingly, the composite cathode delivers a high capacity of 1630.7 mA h g^{-1} and maintains stable capacity retention after 150 cycles at 4 A g^{-1}. The proposed redox catalytic effect sheds light on the tunable Zn–S chemistry.

Received 29th September 2024
Accepted 15th November 2024

DOI: 10.1039/d4sc06593j

rsc.li/chemical-science

1 Introduction

Aqueous zinc–sulfur (Zn–S) batteries feature the merits of being cost-efficient, high theoretical energy density, and non-toxicity, and have been considered as one of the candidates for the next generation of energy storage equipment. Although achievements have been made in Zn–S batteries, their notorious problems have hampered their further development.[1–4] Specifically, the inherent low conductivity of sulfur and its discharge product ZnS greatly jeopardize the redox kinetics, thereby offering an inferior electrochemical response and limited utilization of active materials.[5–7] Furthermore, during the zincation process, the significant expansion of the sulfur species could inflict mechanical damage on the electrode, further deteriorating the cycling performance.

To solve the above-mentioned problems, some strategies have been developed. For example, recent studies indicate that carbon-based materials supported by sulfur are promising cathode materials for Zn–S batteries, but the nonpolar carbon matrix fails to promote the redox kinetics of sulfur. Thus, one can further incorporate the electrocatalytic sites and/or components (*e.g.*, metal oxides) into the composites to facilitate the redox kinetics of sulfur species, thereby endowing the battery with a higher reversible capacity.[8–15] However, for the metal-based catalytic components, it is usually difficult to achieve uniform dispersion in the carbon matrix. In this context, metal–organic frameworks (MOFs) have attracted much attention due to their high porosity, large surface area, and uniform distribution of metal centers and organic ligands at the molecular level.[16,17] After heat treatment, a composite of the carbon matrix with a uniform distribution of metal oxides can be obtained (*i.e.*, catalytic sites), which has the potential to act as the functional matrix for hosting sulfur. Moreover, most reported studies usually focus on accelerating the one-direction conversion (reduction or oxidation) of sulfur, which cannot realize the high utilization of active materials.[18,19] Therefore, it is significant to explore comprehensive cathode materials with bidirectional catalysis for sulfur conversion.

In this contribution, a composite sulfur cathode composed of V_2O_5 and porous carbon (VOC/S) has been prepared by an *in*

[a]*School of Materials Science and Engineering, Xiamen University of Technology, Xiamen 361024, China. E-mail: luohao_hit@163.com*

[b]*College of Chemistry and Chemical Engineering, Qingdao University, Qingdao 266071, China. E-mail: malina@qdu.edu.cn*

[c]*State Key Laboratory of Polymer Materials Engineering, Polymer Research Institute, Sichuan University, Chengdu 610065, P.R. China. E-mail: xiaolongli@scu.edu.cn*

[d]*School of Materials Science and Engineering, Beijing University of Chemical Technology, Beijing, 100029, China. E-mail: mingliw2000@163.com*

[e]*School of Materials Science and Engineering, Zhengzhou University, Zhengzhou 450001, China*

† Electronic supplementary information (ESI) available. See DOI: https://doi.org/10.1039/d4sc06593j

‡ These authors contributed equally to this work.

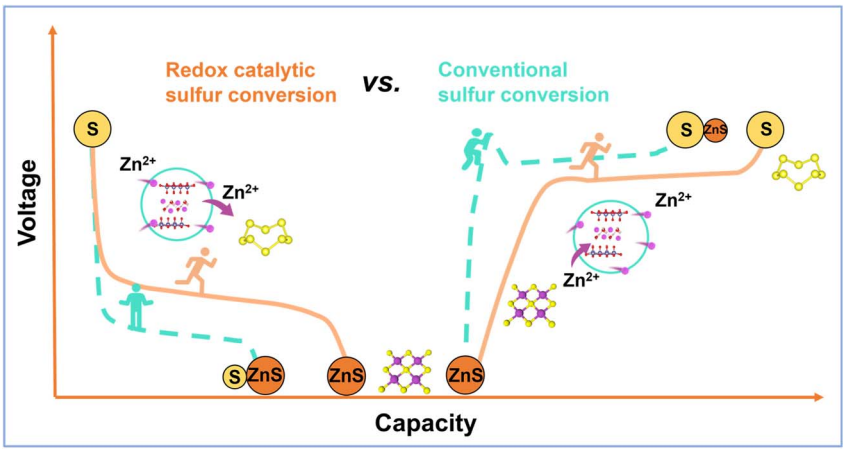

Scheme 1 Schematic illustration of different sulfur speciation pathways enabled by the different matrices.

situ electrochemical-induction strategy, in which the inactive V_2O_3 component is converted to sulphophilic $V_2O_{5-m}\cdot nH_2O$. Benefiting from a unique two-electron redox reaction during the (de) zincification process, the $Zn_xV_2{}^{3+/5+}O_5$ hotspots can serve as a redox medium to invoke the redox catalytic effect for tuning the bidirectional sulfur redox (Scheme 1), thereby greatly enhancing the electrochemical performance of the Zn–S batteries. Accordingly, a highly reversible discharge capacity of 1630.7 mA h g^{-1} and excellent cycling stability can be achieved. This work sheds light on the feasibility of redox catalysis in tuning the sulfur speciation pathway toward high-performance Zn–S batteries.

2 Results and discussion

2.1 Design and characterization of the functional host

Fig. 1a demonstrates the schematic formation process of the V_2O_3@C/S precursor. In a typical procedure, the vanadium-based metal–organic framework (V-MOF) was prepared by the solvothermal method,[20] which showed a cube structure with a variable length (Fig. S1†). After carbonization, the organic component was decomposed into the carbon matrix with a porous structure while the V-centers were oxidized to V_2O_3, which overall led to the transformation of the V-MOF into the vanadium-based oxide and carbon composite materials (V_2O_3@C). Of note, to ensure that the V_2O_3@C inherited the morphological characteristics of the V-MOF without the structure collapsing, we chose to heat the vanadium-based MOFs at a slow heating rate (2 °C min^{-1}) up to 700 °C and keep them there for 4 h to obtain the V_2O_3-containing porous carbon materials (Fig. S2†). Then, the active sulfur was encapsulated into the V_2O_3@C matrix (V_2O_3@C/S) through a conventional melting-diffusion method and the cube structure was retained well, which also realized a sulfur loading of 35 wt% (Fig. 1b and S3†). As shown in Fig. 1c, the high-resolution transmission electron microscopy (HR-TEM) images displayed the lattice fringes of 0.29 nm and 0.32 nm, corresponding to the (104) plane of V_2O_3 and the (206) plane of sulfur (Fig. 1d).[21] The crystalline structure of V_2O_3@C/S was also analyzed by the X-ray diffraction (XRD) technique, and the corresponding results agreed well with the above TEM analysis (Fig. S4†). Furthermore, energy dispersive X-ray spectroscopy (EDS) mapping of V_2O_3@C/S unveiled the homogeneous dispersion of the sulfur element within the carbon scaffold (Fig. 1e). And the overlapping of the C and V elements also confirmed the uniform distribution of vanadium oxides, which is beneficial for facilitating the sulfur redox conversion. The surface characteristics and pore structure of V_2O_3@C before and after sulfur impregnation were evaluated by nitrogen adsorption–desorption measurements (Fig. 1f). V_2O_3@C possesses a high specific surface area of about 201.3 m^2 g^{-1} and a mesopore dominant structure (Table S1†), which can achieve a relatively high sulfur loading while maintaining a good balance of electrochemical performance.[22] After sulfur loading, the sharp decrease in the specific surface area and pore size confirmed the encapsulation of sulfur into the nanopores of V_2O_3@C (Fig. S5†). The above results reveal the successful synthesis of the V_2O_3@C matrix and the good encapsulation of sulfur.

The low valence state of V and the insufficient active sites in V_2O_3 motivated us to further activate its activity by increasing the valence state of vanadium species. Thus, the *in situ* electrochemical induction strategy was employed to reconstruct the phase of V_2O_3 in V_2O_3@C. As shown in Fig. 2a, the V_2O_3@C electrodes underwent electrochemical oxidation during the first charge process as revealed by the high initial charge capacity, suggesting the transformation of V_2O_3@C into V_2O_5@C (VOC). It is worth noting that the phase conversion of vanadium oxides is irreversible because the highly efficient anodic oxidation of V_2O_3@C was achieved only during the first charging process. Correspondingly, as shown in the CV curves of VOC (Fig. 2b), an obvious oxidation peak at ~1.27 V appeared during the first positive scan and then disappeared in the subsequent cycles, which indicates the irreversible electrochemical oxidation of V_2O_3 and also consistent with the charge–discharge curves in Fig. 2a. Furthermore, during the subsequent cycles, two redox peaks at ~1.09/1.1 V and ~0.55/0.74 V were found to be in good agreement with the redox peaks of V^{5+}/V^{4+} and V^{4+}/V^{3+}, which further indicated the formation of V_2O_5.[20] To further explore the

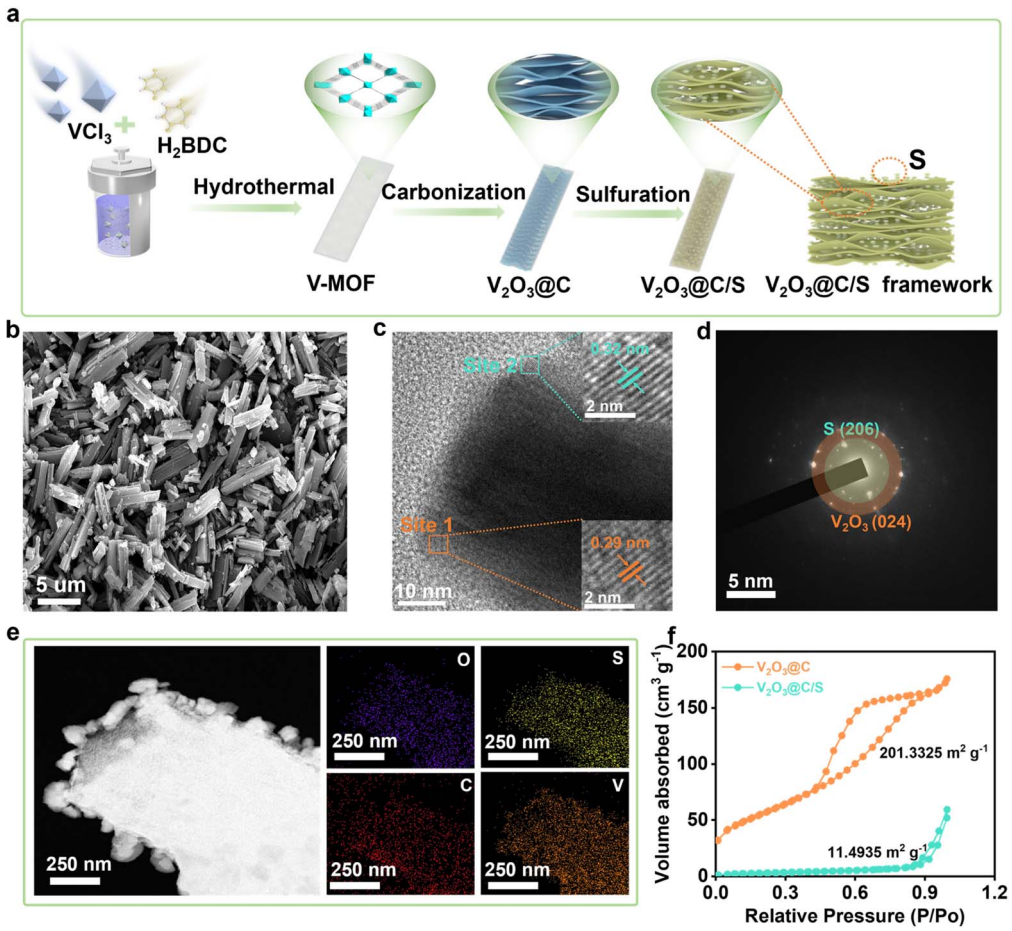

Fig. 1 Structural and compositional characterization of the as-prepared V_2O_3@C/S precursor. (a) Schematic illustration of the synthesis procedure for the V_2O_3@C/S composite. (b) SEM images of V_2O_3@C/S. (c) TEM images of V_2O_3@C/S. (d) SAED pattern of V_2O_3@C/S. (e) SEM image of V_2O_3@C/S and corresponding elemental mappings. (f) Nitrogen adsorption–desorption isotherms of different samples.

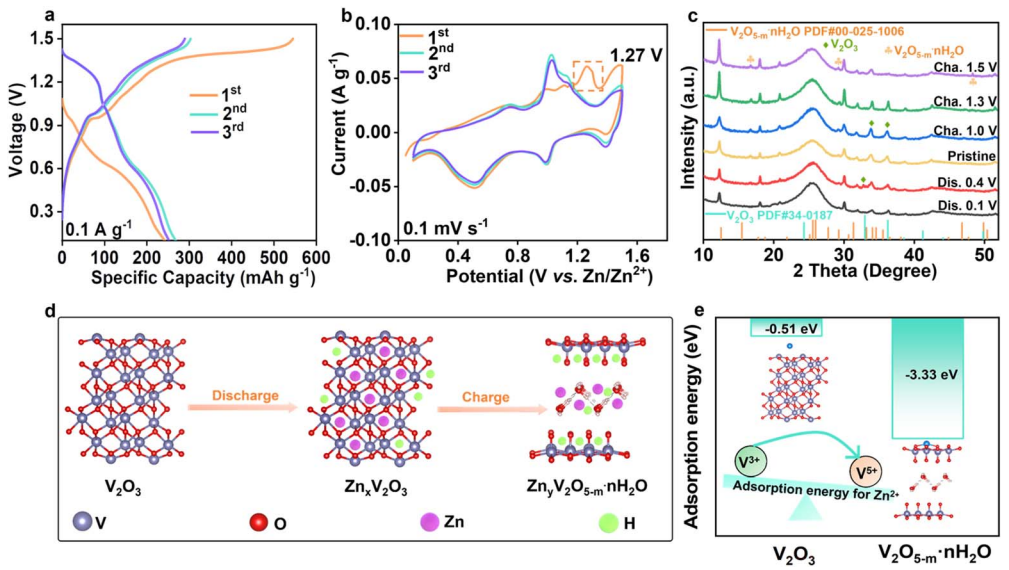

Fig. 2 *In situ* electrochemical reconstruction of the phase of vanadium oxides. (a) Galvanostatic charge/discharge curves of VOC at a current density of 0.1 A g^{-1}. (b) CV curves of VOC at 0.1 mV s^{-1}. (c) XRD patterns of the VOC cathode at different states. (d) Schematic illustration of the oxidation of V_2O_3 during the first cycle. (e) Adsorption energies of V_2O_3 and $V_2O_{5-m}\cdot nH_2O$ towards zinc ions.

structural evolution of VOC during the initial discharge/charge cycle, XRD patterns at different voltages were collected (Fig. 2c). When the VOC cathode is recharged to 1.5 V, a peak of $V_2O_{5-m}\cdot nH_2O$ appears (JCPDS no. 00-025-1006) while the characteristic peak moves slightly to the left, indicating the expanded lattice spacing. As summarized in Fig. 2d, the phase transformation from V_2O_3 to $V_2O_{5-m}\cdot nH_2O$ occurs during the first charging process, and the VOC then functions as the cathode for hosting the ion (de)intercalation in subsequent cycles. Moreover, it is worth mentioning that the *in situ* formed $V_2O_{5-m}\cdot nH_2O$ has faster ion (de)intercalation kinetics and a higher ion storage capacity than commercial V_2O_5. And, the lattice water within the $V_2O_{5-m}\cdot nH_2O$ can act as a pillar to maintain the stability of the layered V_2O_5, thus potentially enhancing the durability of the catalytic matrix.[23,24] Theoretical calculations were also employed to verify the activity of two types of vanadium oxides toward zinc ion storage. As shown in Fig. 2e, adsorption energies of V_2O_3 and $V_2O_{5-m}\cdot 2.4H_2O$ towards Zn^{2+} are calculated, and it is found that the adsorption energy of $V_2O_{5-m}\cdot nH_2O$ (−3.33 eV) is much higher than that of V_2O_3 (−0.51 eV). This difference may be ascribed to the more exposed negatively charged O of the layered $V_2O_{5-m}\cdot nH_2O$ that shows stronger adsorption ability toward zinc ions. This result indicates that $V_2O_{5-m}\cdot nH_2O$ could play a key role in facilitating reversible sulfur conversion by accelerating zinc transport.

2.2 Cation reservoir-mediated redox catalytic sulfur speciation pathway

As discussed above, the VOC functional matrix has shown merits for hosting active sulfur. To directly reflect the matrix-dependent sulfur redox behavior, cyclic voltammetry (CV) curves of Zn–S cells assembled with different cathodes were compared in Fig. 3a. The bare VOC matrix exhibits two pairs of redox peaks, which correspond to the conversion between V^{5+} and V^{3+}. It was identified that the potential of reduction peaks for VOC was higher than that of S/C and the oxidation potential was lower, indicating that the produced $Zn_xV_2{}^{3+/5+}O_5$ possessed the spontaneous redox catalytic activity toward sulfur species during discharge/charge cycling. Specifically, the pre-encapsulated Zn^{2+} ions within the interlayer of VOC transfer from $Zn_{x+1}V_2{}^{3+}O_5$ to the sulfur component *via* a spontaneous chemical reaction ($Zn_{x+1}V_2O_5 + S = Zn_xV_2O_5 + ZnS$, $\Delta G = -6.4$ kJ mol^{-1}).[25] For the charging process, the reoxidation of ZnS is realized by $Zn_xV_2{}^{5+}O_5$ ($Zn_xV_2O_5 + ZnS = Zn_{x+1}V_2O_5 + S$, $\Delta G = -7.02$ kJ mol^{-1}), which overall facilitates the reversible bidirectional sulfur speciation pathway. The VOC/S cathode indeed exhibited small polarization and higher response current compared with the S/C cathode, suggesting accelerated redox kinetics and efficient sulfur conversion. We then conducted galvanostatic charge/discharge (GCD) tests to verify the improved sulfur utilization and redox kinetics. As expected, the VOC/S cathode delivered better redox kinetics and efficient sulfur conversion, as indicated by its lower voltage polarization and high capacity compared with the S/C cathode (Fig. 3b). The specific capacity of VOC/S reached 1630.73 mA h g^{-1} at 0.2 A g^{-1} and a low polarization of 0.55 V. Of note, for the reverse charging process, the VOC/S cathode displayed a lower charging voltage plateau and activation potential, suggesting the facile ZnS reoxidation process. Such a result confirms that the redox

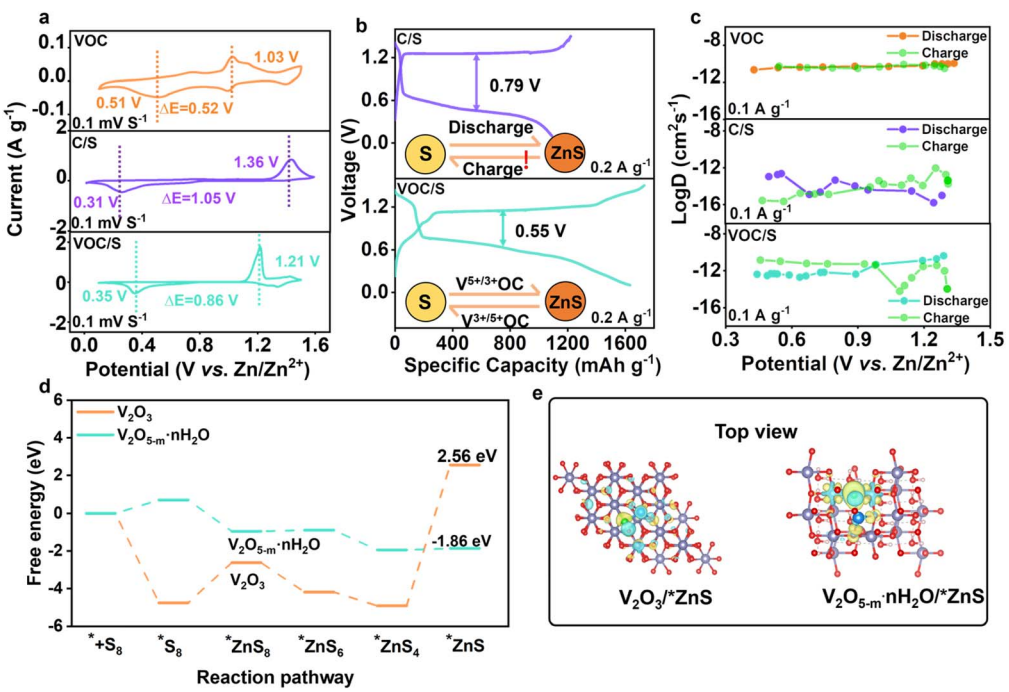

Fig. 3 Mechanistic investigation on the redox catalysis facilitated sulfur conversion and DFT results. (a) CV curves of different cathodes as noted. (b) GCD profiles of C/S and VOC/S cathodes. (c) GITT curves of different cathodes. (d) Gibbs free energy for the sulfur reduction path. (e) Top views of the charge density distribution of V_2O_3 and $V_2O_{5-m}\cdot nH_2O$ with decomposition in the *ZnS adsorption system.

catalytic effect invoked by the vanadium active centers could significantly accelerate the bidirectional sulfur conversion.

Then, the galvanostatic intermittent titration technique (GITT) was employed to determine the diffusion coefficient of Zn^{2+}(D_{Zn}) thereby revealing the origin of the improved redox kinetics (Fig. S6†).[26–31] As shown in Fig. 3c, the calculated D_{Zn} of VOC was as high as 10^{-12} to 10^{-9} cm^2 s^{-1}, which is higher than that of the S/C cathode, suggesting the substantially faster Zn^{2+} (de)insertion kinetics of $V_2O_{5-m}\cdot nH_2O$ than sulfur species. Accordingly, the VOC/S cathode indeed exhibited higher D_{Zn} than the S/C cathode, which confirms the accelerated cation transport enabled by the VOC matrix. This also suggests that V_2O_5 served as a cation reservoir for rapid Zn^{2+} transfer, endowing the VOC/S cathode with significantly enhanced redox kinetics. To further validate the catalytic activity of V_2O_5 towards sulfur conversion at the molecular or atomic scale, the Gibbs free energies of each zincification step were calculated and are described in Fig. 3d. As shown, the rate-determining step for the whole reduction process was identified as the conversion of *ZnS_4 to *ZnS.[32,33] Compared with V_2O_3, V_2O_5 possesses a lower free energy of 1.86 eV, indicating more efficient sulfur conversion. Furthermore, the charge density distribution of ZnS adsorbed on different matrices was calculated to reveal the electron transport properties in this work. As shown in Fig. 3e, it can be noted that the charge density between $V_2O_{5-m}\cdot nH_2O$ and ZnS was richer, indicating the formation of an electron conduction pathway between $V_2O_{5-m}\cdot nH_2O$ and polysulfide. Such electron transport could enable the V_2O_5 sites to better utilize their intrinsic catalytic properties.

2.3 Electrochemical performance of aqueous Zn–S batteries

To validate the accessibility of the as-prepared VOC/S cathode, the rate performance of the as-prepared Zn–S cells was evaluated. The VOC/S cathode indeed exhibits an excellent rate performance of 1040–422 mA h g^{-1} at current densities ranging from 1–10 A g^{-1}, substantially better than that of the S/C cathodes. Note that the reversible capacity of the VOC/S cathode retains over 40% of its initial value when the current density increases 10 times from 1 to 10 A g^{-1}, suggesting that the V_2O_5 components could substantially accelerate the ion transport. The corresponding GCD profiles of VOC/S at various current densities are presented in Fig. S7,† in which these voltage plateaus are visible and the polarization increases slowly, further indicating superior redox kinetics.

Of note, the cycling stability of aqueous Zn–S batteries is a critical issue because the sluggish redox kinetics and irreversible sulfur conversion would cause the fast capacity fade. Interestingly, the VOC/S//Zn cell delivers a good capacity retention of 82% after 50 cycles at a current density of 2 A g^{-1} (Fig. 4b), while the C/S//Zn cell nearly loses its capacity. Such strong differences highlight that the redox catalytic effect enabled by the VOC matrix could significantly improve the reversibility of bidirectional sulfur conversion. Note that the irreversible side reaction (*e.g.* $2ZnS + 4H_2O + 10e^- \rightarrow 2Zn^{2+} + SO_4^{2-} + S + 8H^+$) during battery recharging is the main reason for the relatively low coulombic efficiency (CE) of the VOC/S//Zn cell.[34]

After further cycling at a high current density of 4 A g^{-1}, the VOC/S cathode can still obtain a capacity retention rate of 71.52% after 150 cycles (Fig. 4c), and the coulombic efficiency is nearly 100%. Moreover, it can be observed that there was almost no capacity attenuation in the VOC/S cathode during the first 30 cycles (Fig. S8†). Electrochemical impedance spectra of the cathodes before and after cycling were collected, in which the VOC/S cathode still maintained a low internal resistance compared with the C/S cathode, indicating that the VOC matrix

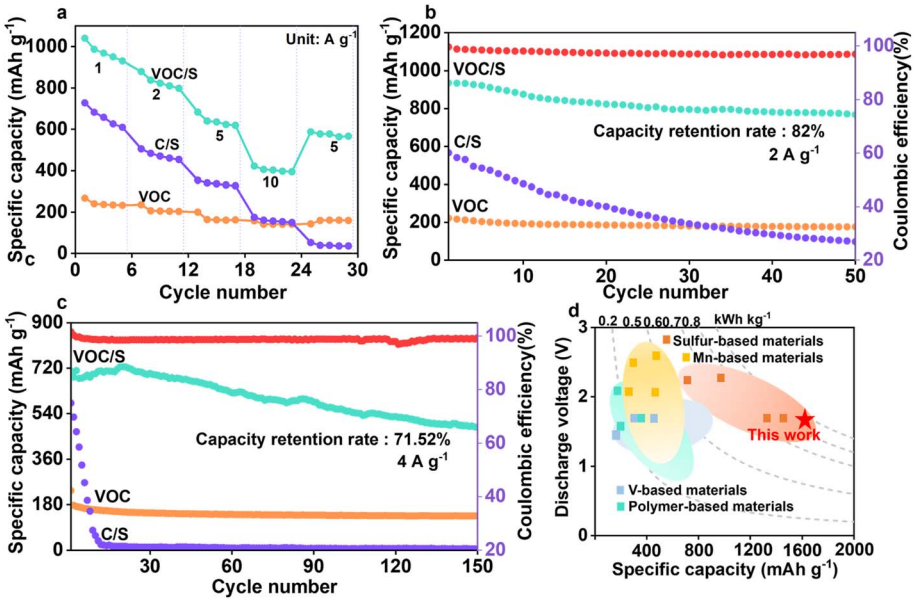

Fig. 4 Electrochemical performance of the VOC/S cathode. (a) Rate performance. Cycle performance at a current density of (b) 2 A g^{-1} and (c) 4 A g^{-1}. (d) Electrochemical performances of our work compared with those of previously reported aqueous Zn-ion batteries.

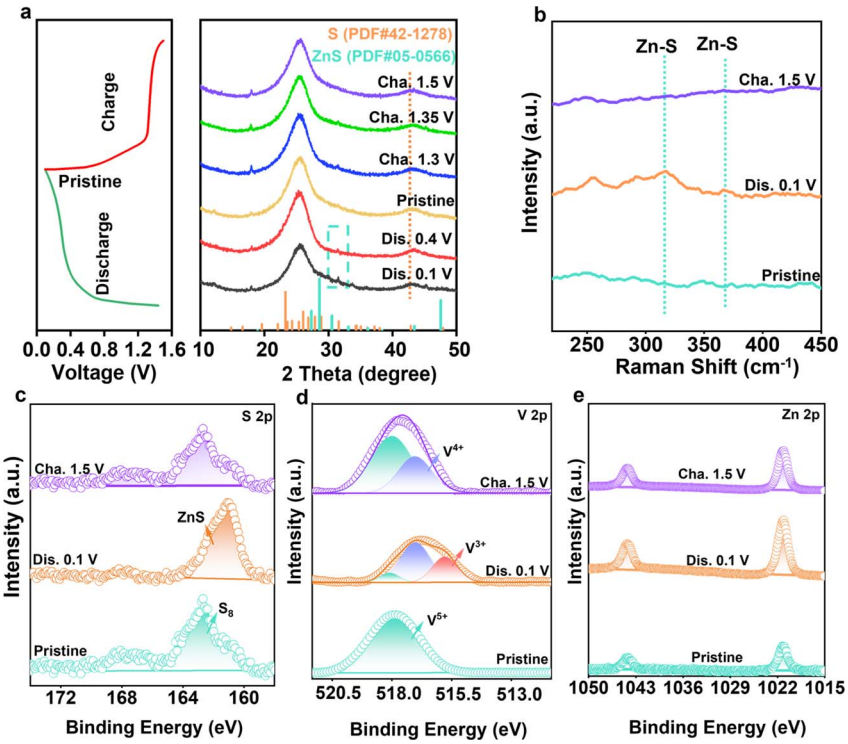

Fig. 5 Analysis of reversible sulfur redox conversion. (a) *Ex situ* XRD patterns collected at different states. (b) Raman spectra at different charge and discharge states. XPS spectra of (c) S 2p, (d) V 2p, and (e) Zn 2p at different states.

greatly enhances redox kinetics (Fig. S9†). Moreover, the cycled C/S cathode displayed more agglomeration after cycling compared with the fresh C/S cathode, while the VOC/S cathode retained a relatively complete structure, confirming its structural stability (Fig. S10†). Such structural robustness enables the as-prepared Zn–S cells with a long cycling life. These results suggest that the V_2O_5 cation reservoir plays a key role in facilitating the ion transfer and also demonstrates the robustness of the VOC matrix.

A proof-of-concept Zn–S pouch cell was assembled to further validate the application potential of the VOC/S cathode (Fig. S11†). The as-prepared pouch cell could brighten a small light bulb and run a fan, demonstrating its promise in real applications. Fig. 4d also compares the overall electrochemical performance of this work with the reported results, which is comparable to or even better than that of previously reported literature data.[35–48]

2.4 Investigation of the reversible sulfur redox conversion

To reveal the Zn^{2+} ion storage mechanism, the phase changes of the VOC/S cathode were recorded. Fig. 5a displays the XRD patterns of VOC/S electrodes at different charge/discharge states. The characteristic peak of ZnS gradually became obvious during discharge, while the peak gradually decreased during the charging process, indicating the reversible conversion between ZnS and S.[49–52] Of note, during one charge/discharge cycle (Fig. 5b), the vibrational Raman peaks of Zn–S also followed the same trend with the XRD results, further confirming the reversible sulfur speciation paths. Such complete sulfur conversion originates from the V-redox couple accelerated redox kinetics. Thus, the valence-state changes of the VOC/S cathode were further inspected to demonstrate the reason for the origin of the reversible sulfur conversion reactions. As shown in Fig. 5c, the original state (163.0 and 167.48 eV) can be assigned to S_8. When discharged to 0.1 V, a new peak (161.2 eV) appears, representing ZnS. After recharging to 1.5 V, the peak corresponding to S_8 is the same as the original state, further confirming the complete reversible sulfur conversion. The vanadium oxides function as the cation reservoir that can accommodate fast zinc ion transport.[53–56] During the battery discharging process, the reduction of $Zn_xV_2{}^{5+}O_5$ and sulfur with the formation of $Zn_{x+1}V_2{}^{3+}O_5$ and ZnS takes place simultaneously (Fig. 5d and e). The pre-zincified $Zn_{x+1}V_2{}^{3+}O_5$ could integrate zinc ions with sulfur, thereby facilitating the sulfur reduction kinetics. For reverse charging, the vanadium-active centers enable facile ZnS reoxidation, overall enabling the one-step reversible conversion between sulfur and ZnS.

3 Conclusion

In summary, an *in situ* reconstruction strategy was developed to fabricate a catalytic matrix for hosting sulfur species and tune its conversion pathway. The phase transition process of the VOC was analyzed by systematic spectroscopic techniques and electrochemical tests, while the theoretical results revealed that the V_2O_5 features more merits for facilitating sulfur conversion. Therefore, the as-prepared V_2O_5 functions as a cation-transport medium, which can direct the reversible sulfur conversion.

Specifically, the zincified $Zn_xV_2^{3+/5+}O_5$ redox couple served as the cation reservoir to enable redox catalytic reversible sulfur conversion during dynamic battery discharge–charge. Consequently, the as-obtained sulfur cathode exhibits a lower voltage hysteresis of 0.55 V, a high discharge capacity of 1630.7 mA h g^{-1}, and an excellent rate performance of 422 mAh g^{-1} at 10 A g^{-1}. This work demonstrates a new avenue for manipulating sulfur redox, which could unlock the full potential of aqueous zinc–sulfur batteries.

Data availability

Data will be made available on request.

Author contributions

Hao Luo and Fan Li contributed equally to this work. Hao Luo: conceptualization, funding acquisition, writing-review & editing. Fan Li: investigation, writing-original draft. Mingli Wang: conceptualization, investigation, writing-original draft. Shang Sun: investigation, formal analysis. Min Zhou: writing-review & editing. Wenjing Zhang: formal analysis, investigation. Hengrui Guo: investigation, methodology. Xueyin Su: formal analysis, methodology. Xiaolong Li: methodology, writing-review & editing. Lina Ma: conceptualization, funding acquisition, resources.

Conflicts of interest

The authors declare no conflict of interest.

Acknowledgements

This study was financially supported by the China Postdoctoral Science Foundation (Grant No. 2022TQ0282), the Natural Science Foundation of Fujian Province, China (No. 2024J011210) the High-level talent start-up Foundation of Xiamen Institute of Technology (grant No. YKJ23017R), and the Natural Science Foundation of Shandong Province of China (No. ZR2023QE071).

References

1 M. L. Wang, H. Zhang, W. L. Zhang, Q. W. Chen and K. Lu, *Small Methods*, 2022, **6**, 2200335.
2 L. K. Hencz, H. Chen, Z. Z. Wu, S. S. Qian, S. Chen, X. X. Gu, X. H. Liu, C. Yan and S. Q. Zhang, *Exploration*, 2022, **2**, 20210131.
3 H. Zhang, B. Song, W. W. Zhang, B. An, L. Fu, S. T. Lu, Y. W. Cheng, Q. W. Chen and K. Lu, *Angew. Chem., Int. Ed.*, 2023, **62**, e202217009.
4 X. L. Li, N. Li, Z. D. Huang, Z. Chen, G. J. Liang, Q. Yang, M. Li, Y. W. Zhao, L. T. Ma, B. B. Dong, Q. Huang, J. Fan and C. Y. Zhi, *Adv. Mater.*, 2021, **33**, 2006897.
5 M. Salama, Rosy, R. Attias, R. Yemini, Y. Gofer, D. Aurbach and M. Noked, *ACS Energy Lett.*, 2019, **4**, 436–446.
6 H. Zhang, Z. T. Shang, G. Luo, S. H. Jiao, R. G. Cao, Q. W. Chen and K. Lu, *ACS Nano*, 2022, **16**, 7344–7351.
7 D. D. Liu, B. He, Y. Zhong, J. Chen, L. X. Yuan, Z. Li and Y. H. Huang, *Nano Energy*, 2022, **101**, e107474.
8 R. H. Gao, M. T. Zhang, Z. Y. Han, X. Xiao, X. R. Wu, Z. H. Piao, Z. J. Lao, L. Nie, S. G. Wang and G. M. Zhou, *Adv. Mater.*, 2024, **36**, 2303610.
9 H. Li, M. Y. Chuai, X. Xiao, Y. Y. Jia, B. Chen, C. Li, Z. H. Piao, Z. G. Lao, M. T. Zhang, G. H. Gao, B. K. Zhang, Z. Y. Han, J. L. Yang and G. M. Zhou, *J. Am. Chem. Soc.*, 2023, **145**, 22516–22526.
10 K. Lu, H. Zhang, S. Y. Gao, H. Y. Ma, J. Z. Chen and Y. W. Cheng, *Adv. Funct. Mater.*, 2019, **29**, 1807309.
11 B. Q. Li, H. J. Peng, X. Chen, S. Y. Zhang, J. Xie, C. X. Zhao and Q. Zhang, *CCS Chem.*, 2019, **1**, 128–137.
12 V. Marangon, C. Hernández-Rentero, M. Olivares-Marín, V. Gómez-Serrano, Á. Caballero, J. Morales and J. Hassoun, *ChemSusChem*, 2021, **14**, 3333.
13 A. Manthiram, Y. Z. Fu, S.-H. Chung, C. X. Zu and Y.-S. Su, *Chem. Rev.*, 2014, **114**, 11751–11787.
14 R. Wang, S. Xin, D. L. Chao, Z. X. Liu, J. D. Wan, P. Xiong, Q. Q. Luo, K. Hua, J. N. Hao and C. F. Zhang, *Adv. Funct. Mater.*, 2022, **32**, 2207751.
15 Y. Yang, H. J. Yang, R. J. Zhu and H. S. Zhou, *Energy Environ. Sci.*, 2023, **16**, 2723–2731.
16 X. Wang, L. Y. Liu, Z. W. Hu, C. C. Peng, C. Han and W. J. Li, *Adv. Energy Mater.*, 2023, **13**, 2302927.
17 K. N. Wang, J. W. Wang, Z. Q. Zhang, W. L. Zhang, F. Feng and Y. P. Du, *Sci. China: Chem.*, 2023, **66**, 2711–2718.
18 L. L. Feng and S. P. Wang, *Sci. China: Chem.*, 2023, **66**, 2267–2273.
19 P. Zeng, H. Zou, C. Cheng, L. Wang, C. Yuan, G. L. Liu, J. Mao, T.-S. Chan, Q. Y. Wang and L. Zhang, *Adv. Funct. Mater.*, 2023, **33**, 2214770.
20 H. Luo, B. Wang, F. Wang, J. Yang, F. D. Wu, Y. Ning, Y. Zhou, D. L. Wang, H. K. Liu and S. X. Dou, *ACS Nano*, 2020, **14**, 7328–7337.
21 S. S. Tan, Y. L. Jiang, Q. L. Wei, Q. M. Huang, Y. H. Dai, F. Y. Xiong, Q. D. Li, Q. Y. An, X. Xu, Z. Z. Zhu, X. D. Bai and L. Q. Mai, *Adv. Mater.*, 2018, **30**, 1707122.
22 Y. R. Qi, Q.-J. Li, Y. K. Wu, S.-J. Bao, C. M. Li, Y. M. Chen, G. X. Wang and M. W. Xu, *Nat. Commun.*, 2021, **12**, 6347.
23 D. Kundu, B. Adams, V. Duffort, S. H. Vajargah and L. Nazar, *Nat. Energy*, 2016, **1**, 1611.
24 M. Y. Yan, P. He, Y. C, S. Y. W, Q. L. W, K. N. Zhao, X. Xu, Q. Y. An, Y. Shuang, Y. Y. Shao, K. T. Mueller, L. Q. Mai, J. Liu and J. H. Yang, *Adv. Mater.*, 2017, 1703725.
25 X. Y. Wu, A. Markir, L. Ma, Y. K. Xu, H. Jiang, D. P. Leonard, W. Shin, T. P. Wu, J. Lu and X. L. Ji, *Angew. Chem., Int. Ed.*, 2019, **58**, 12640.
26 Y. C. Chien, H. D. Liu, A. S. Menon, W. R. Brant, D. Brandell and M. J. Lacey, *Nat. Commun.*, 2023, **14**, 2289.
27 W. Wang, Y. Tang, J. Liu, H. B. Li, R. Wang, L. H. Zhang, F. Liang, W. Bai, L. Zhang and C. F. Zhang, *Chem. Sci.*, 2023, **14**, 9033–9040.

28 R. Wang, Q. W. Ma, L. H. Zhang, Z. X. Liu, J. D. Wan, J. F. Mao, H. B. Li, S. L. Zhang, J. N. Hao, L. Zhang and C. F. Zhang, *Adv. Energy Mater.*, 2023, **13**, 2302543.
29 H. J. Yang, R. J. Zhu, Y. Yang, Z. Y. Lu, Z. Chang, P. He, C. Y. Zhu, S. Kitano, Y. Aoki, H. Habazaki and H. S. Zhou, *Energy Environ. Sci.*, 2023, **16**, 2133–2141.
30 Y. Yang, W. H. Yang, R. J. Zhu, G. Wu, Y.-K. Choe, K. Sho, H. J. Yang and E. Yoo, *Energy Storage Mater.*, 2024, **72**, 103691.
31 Y. Yang, R. J. Zhu, G. Wu, W. H. Yang, H. J. Yang and E. Yoo, *ACS Nano*, 2024, **18**, 19003–19013.
32 W. J. Xue, Z. Shi, L. M. Suo, C. Wang, Z. Q. Wang, H. Z. Wang, K. P. So, A. Maurano, D. W. Yu and Y. M. Chen, *Nat. Energy*, 2019, **4**, 374–382.
33 W. L. Wu, S. B. Wang, L. Lin, H.-Y. Shia and X. Q. Sun, *Energy Environ. Sci.*, 2023, **16**, 4326.
34 M. L. Wang, H. Zhang, T. H. Ding, F. J. WuL. Fu, B. Song, P. F. Cao and K. Lu, *Sci. China Chem.*, 2024, **67**, 1531–1538.
35 Y. Q. Guo, R. Chua, Y. Q. Chen, Y. Cai, E. J. J. Tang, J. J. N. Lim, T. H. Tran, V. Verma, M. W. Wong and M. Srinivasan, *Small*, 2023, **19**, 2207133.
36 Y. C. Ding, Y. Q. Peng, S. H. Chen, X. X. Zhang, Z. Q. Li, L. Zhu, L.-E. Mo and L. H. Hu, *ACS Appl. Mater. Interfaces*, 2019, **11**, 44109–44117.
37 C. Sun, J. H. Zhu, B. Liu, M. W. Xu, J. Jiang and T. Yu, *ACS Energy Lett.*, 2023, **8**, 772–779.
38 Z. D. Yang, B. Y. Wang, Y. J. Chen, W. H. Zhou, H. P. Li, R. Z. Zhao, X. R. Li, T. S. Zhang, F. X. Bu, Z. W. Zhao, W. Li, D. L. Chao and D. Y. Zhao, *Natl. Sci. Rev.*, 2023, **10**, nwac268.
39 K. K. Sonigara, J. V. Vaghasiya, C. C. Mayorga-Martinez C and P. Martin, *npj 2D Mater. Appl.*, 2023, **7**, 45.
40 Y. Fei and G. Li, *Adv. Funct. Mater.*, 2024, **34**, 2312550.
41 Y. X. Li, Y. Lu, Y. X. Ni, S. B. Zheng, Z. H. Yan, K. Zhang, Q. Zhao and J. Chen, *J. Am. Chem. Soc.*, 2022, **144**, 8066–8072.
42 X. X. Jia, C. F. Liu, Z. Wang, D. Huang and G. Z. Cao, *Nano-Micro Lett.*, 2024, **16**, 129.
43 Y. F. Huang, Y. Z. Peng, Q. Ouyang, Q. Feng, H. Wang, D. Z. Zheng, F. X. Wang, X. H. Lu and Q. Liu, *Energy Storage Mater*, 2024, **70**, 103476.
44 J. L. Yang, W. B. Gong and F. X. Geng, *Adv. Funct. Mater.*, 2023, **33**, 2301202.
45 D. X. Geng, H. Zhang, Z. J. Fu, Z. M. Liu, Y. F. An, J. Yang, D. W. Sha, L. Pan, C. Yan and Z. M. Sun, *Adv. Sci.*, 2024, 2407073.
46 S. B. Zheng, D. J. Shi, D. Yan, Q. R. Wang, T. J. Sun, T. Ma, L. Li, D. He, Z. L. Tao and J. Chen, *Angew. Chem., Int. Ed.*, 2022, **61**, e202117511.
47 H. Zhang, D. X. Xu, L. W. Wang, Z. L. Ye, B. Chen, L. Y. Pei, Z. Y. Wang, Z. Y. Cao, J. F. Shen and M. X. Ye, *Small*, 2021, **17**, 2100902.
48 Z. L. Han, S. P. Li, M. J. Sun, R. J. He, W. Zhong, C. Yu, S. J. Cheng and J. Xie, *J. Energy Chem.*, 2022, **68**, 752–761.
49 W. W. Zhang, M. L. Wang, J. K. Ma, H. Zhang, L. Fu, B. Song, S. T. Lu and K. Lu, *Adv. Funct. Mater.*, 2023, **33**, 2210899.
50 M. Yang, Z. C. Yan, J. Xiao, W. L. Xin, L. Zhang, H. L. Peng, Y. H. Geng, J. W. Li, Y. X. Wang, L. Liu and Z. Q. Zhu, *Angew. Chem., Int. Ed.*, 2022, **61**, e202212666.
51 X. Z. Yang, C. Li, Z. T. Sun, S. Yang, Z. X. Shi, R. Huang, B. Z. Liu, S. Li, Y. H. Wu, M. L. Wang, Y. W. Su, S. X. Dou and J. Y. Sun, *Adv. Mater.*, 2021, **33**, 210595.
52 M. J. Chen, Q. Y. Zhao, H. R. Wang, T. Long, X. Ma, Q. Wu, W. X. Zhou, X. W. W and X. X. Zeng, *Sci. China Chem.*, 2023, **66**, 289–296.
53 J. D. Guo, J. X. Liu, W. B. Ma, Z. Y. Sang, L. X. Yin, X. Q. Zhang, H. Chen, J. Liang and D. A. Yang, *Adv. Funct. Mater.*, 2023, **33**, 2302659.
54 T. Zhou, D. Xuan and G. Guo, *J. Energy Chem.*, 2024, **95**, 9–19.
55 Z. Y. Feng, Y. L. Zhang, Z. M. Gao, D. D. Hu, H. M. Jiang and T. Hu, *Adv. Powder Mater.*, 2024, **3**, 100167.
56 Z. H. Song, Y. Zhao, H. R. Wang, A. B. Zhou, X. Y. Jin, Y. X. Huang, L. Li, F. Wu and R. J. Chen, *Energy Environ. Sci.*, 2024, **17**, 6666–6675.